Modeling the nanoindentation response of silicate glasses by peridynamic simulations

Cao, Yuzhe; Kazembeyki, Maryam; Tang, Longwen; Krishnan, N. M.Anoop; Smedskjaer, Morten M.; Hoover, Christian G.; Bauchy, Mathieu

Published in:
Journal of the American Ceramic Society

DOI (link to publication from Publisher):
10.1111/jace.17720

Publication date:
2021

Document Version
Accepted author manuscript, peer reviewed version

PROFESSOR N. M. ANOOP KRISHNAN (Orcid ID : 0000-0003-1500-4947)
DR MORTEN SMEDSKJAER (Orcid ID : 0000-0003-0476-2021)
DR MATHIEU BAUCHY (Orcid ID : 0000-0003-4600-0631)

Article type : Article

Modeling the Nanoindentation Response of Silicate Glasses by Peridynamic Simulations

Yuzhe Cao [a], Maryam Kazembeyki [b], Longwen Tang [a], N M Anoop Krishnan [d,e], Morten M. Smedskjaer[c], Christian G. Hoover [b], and Mathieu Bauchy [a,*]

a Physics of AmoRphous and Inorganic Solids Laboratory (PARISlab), Department of Civil and Environmental Engineering, University of California, Los Angeles, CA 90095, USA
b School of Sustainable Engineering and the Built Environment, Arizona State University, Tempe, AZ 85287, USA
c Department of Chemistry and Bioscience, Aalborg University, Aalborg 9220, Denmark
d Department of Civil Engineering, Indian Institute of Technology Delhi, New Delhi 110016, India
e Department of Materials Science and Engineering, Indian Institute of Technology Delhi, New Delhi 110016, India
* Corresponding author: bauchy@ucla.edu

Keywords:
Soda-lime silicate glass
Nanoindentation
Load-displacement curve
Peridynamics

Abstract

Nanoindentation is a widely used method to probe the mechanical properties of glasses. However, interpreting glasses' response to nanoindentation can be challenging due to the complex nature of the stress field under the indenter tip and the lack of *in situ* characterization techniques. Here, we present a numerical model describing the nanoindentation of an archetypical soda-lime silicate window glass by means of peridynamic simulations. We show that, although it does not capture shear flow and permanent densification, peridynamics exhibits a good agreement with experimental nanoindentation data and offers a direct access to the stress field forming under the indenter tip.

1. Introduction

Over the past several decades, indentation has been extensively used to characterize the mechanical behaviors of materials.[1–6] The analysis of the load-displacement curves yields the indentation hardness and stiffness of the tested material.[7, 8] However, the nature of the mechanical response of materials upon indentation is complex and depends on (i) the spatial scale of the probed region (e.g., microindentation, nanoindentation, etc.), (ii) the intensity of the load, (iii) the rate of loading/unloading, (iv) the geometry of the indenter tip (e.g., spherical or Hertzian indenter, square pyramidal Vicker's indenter, elongated pyramidal Knoop indenter, triangular Berkovich indenter, etc.), and (v) environmental effects, such as temperature and humidity.[9–15] Given the brittle fracture behavior of oxide glasses, it is of particular interest to test their resistance to surface damage by indentation.[16] Glasses exhibit several behaviors under indentation, including reversible elastic deformation, fracture, volume-conservative shear flow, and permanent densification.[17, 18] Understanding the mechanism, magnitude, and localization of these deformation processes requires an accurate knowledge of the stress field that is generated under the tip upon indentation, which is challenging to access experimentally, especially in real time.[19, 20] These difficulties have inhibited a deep understanding of the behavior of glasses during indentation.

Clearly, numerical modeling offers an ideal complement to experiments to decipher the local response of glasses under the tip. In particular, molecular dynamics (MD) simulations have been applied to model the effect of indentation on various materials.[21–23] However, due to their computational cost, MD simulations are usually unable to capture the spatial and temporal scales associated with indentation tests. The indentation of a variety of materials has also been

investigated by simulation methods based on continuum mechanics, such as the finite element method (FEM).[24–27] However, based on its differential formation of mechanics, classical FEM is unable to properly handle difficulties associated with stress discontinuities, interfaces, and crack initiation and propagation—which may arise upon indentation. Various refinements have been proposed to handle these difficulties within the framework of FEM.[28–30]

Peridynamics offers a convenient, alternative pathway, since, by relying on a non-local, integral formulation of mechanics, peridynamic simulations intrinsically address the difficulties facing FEM. Specifically, crack initiation and propagation can directly be simulated without additional treatments in peridynamics, which makes this approach more flexible to investigate multiple-crack problems.[31–35] As a result, peridynamic simulations offer a promising route to model the mechanical response of glasses subjected to indentation. Although peridynamics has been extensively used to model the mechanical response of materials under several load conditions,[36–38] its application to indentation modeling has remained limited to a few studies,[39–43] However, to the best of our knowledge, the ability of peridynamics to properly describe the response to indentation of oxide glasses is yet to be demonstrated.

Here, to address this issue, we combine nanoindentation testing and peridynamic simulations to model the indentation response of a soda-lime silicate (window) glass, which is by far the most widely produced glass in the world.[44] Here, as a stepping stone toward a more complete, realistic description of glass indentation within the peridynamic framework, we adopt the linear peridynamic solid (LPS) constitutive model to describe the deformation of the soda-lime silicate glass, wherein the solid is assumed to deform in a linear-elastic fashion until failure. This constitutive model solely captures reversible elastic deformations and fracture, without explicitly accounting for shear and permanent densification—two behaviors that are typically observed during glass indentation.[17, 18] Despite the simplicity of this constitutive model, we show that peridynamics yields a good agreement with experiments, both in terms of load-displacement curve and resulting indentation stiffness/hardness. These simulations offer a direct access to the stress field experienced by the glass under indentation.

2. Methods

2.1 Nanoindentation experiments

The nanoindentation tests are performed with a diamond Berkovich tip using an ultrahigh-resolution-nanoindenter (UNHT^3) from Anton Paar.[45] Here, we consider this indenter tip geometry primarily on account of the fact that it is widely used in instrumented indentation tests for glassy materials.[46] This indenter tip has a well-defined area function and calibration function. As compared to other indenters (e.g., four-sided Vickers indenter), the three-sided pyramid shape of the Berkovich indenter can be ground to a point and maintains its self-similar geometry down to very small scales.[47] We select as an archetypical brittle material a commercial soda-lime silicate glass manufactured by VWR Scientific Inc. (typical microscope slide 75 × 25 × 1 mm^3).[48] The glass sample surfaces are smooth and free of imperfections from the manufacturer. All the glass samples are annealed prior to indentation—wherein the thermal profile consists of heating the samples at a rate of 300 K/h up to the annealing temperature (taken here as $0.9 \cdot T_g$, where T_g is the glass transition temperature). In this study, all tests are performed at ambient temperature (~ 20 °C) and relative humidity (from 10-to-15%).[48] It has been shown in previous studies that the hardness of a glass does not solely depends on its composition, but also on the maximum indentation load exerted on the indenter's tip—a phenomenon known as the "indentation size effect" (ISE).[48] Here, to filter out any spurious effect arising from the ISE, we fix the maximum penetration depth at 400 nm for both experiments and simulations. The loading and unloading rate for each indent is fixed at 1.33×10^{-8} m/s and the maximum penetration depth was held constant for a duration time of 10 seconds. For statistical averaging purposes, 50 experimental indents are performed. Figure 1 shows a typical indentation load-displacement curve. After the indentation cycle, we measure the topography of the indented surface by means of atomic force microscopy (AFM) by measuring the vertical height of the residual indentation imprints. The scan is conducted in contact mode at room temperature with an aluminum cantilever tip. We use surface correction and flattening modifications included in the open source software Gwyddion to prepare the AFM images.[48]

2.2 Mechanical properties extracted from nanoindentation

We use the Oliver and Pharr[7] methodology to calculate the hardness (H) and modulus (M) from the load-displacement curves. Hardness is first defined as the ratio of the maximum load (P_{max}) and the projected contact area (A_c):

$$H = \frac{P_{\max}}{A_c(h_c)} \tag{1}$$

where $A_c = 24.56 \cdot h_c^2$ is the projected area shape function for an ideal Berkovich tip and h_c is the contact depth (see Fig. 1). The nanoindentation modulus (M) is then defined in terms of the contact stiffness (S) as:

$$M = \frac{\sqrt{\pi}}{2} \frac{S}{\sqrt{A_c(h_c)}} \tag{2}$$

where $S = dP/dh$ is the initial slope of the load-displacement curve upon unloading, calculated at the maximum penetration depth.

2.3 Peridynamics theory

Rather than using the classical FEM approach (based on a local theory), we herein adopt peridynamics to model the nanoindentation process. Indeed, rather than relying on partial differential equations as in classical FEM,[49] peridynamics is based on a non-local, integral formulation of mechanics (i.e., integral equations). Such integral formulations can conveniently handle difficulties related to stress discontinuities.[50] Furthermore, the initiation and propagation of cracks can naturally be taken into consideration, without additional treatments. This makes peridynamics a promising method to model indentation.

In peridynamics, the simulated material is discretized into a series of points **x**. Each point **x** then interacts with neighboring points **x'** within a specific region, which is known as the horizon of **x** ($H_{\mathbf{x}}$), i.e., is a sphere centered around **x** and of radius δ. The equation of motion can be written as:

$$\rho\ddot{\mathbf{u}}(\mathbf{x};\mathrm{t}) = \int_{H_x} \mathbf{T}[\mathbf{u}(\mathbf{x}', t) - \mathbf{u}(\mathbf{x}, t), \mathbf{x}' - \mathbf{x}]\mathbf{dx}' + \boldsymbol{b}(\mathbf{x},t) \tag{3}$$

where **u** is the displacement vector, ρ is the local density, ü denotes the second derivative with respect to time of **u**, **T** is the peridynamic force vector state that describes the interaction between

pairs of points $\mathbf{x}$ and $\mathbf{x}'$, and $\boldsymbol{b}$ is the total body force density. The relative position $\boldsymbol{\xi}$ of two material points is defined as:

$$\boldsymbol{\xi} = \mathbf{x}' - \mathbf{x} \tag{4}$$

and the corresponding relative displacement $\boldsymbol{\eta}$ is defined as:

$$\boldsymbol{\eta} = \mathbf{u}(\mathbf{x}', t) - \mathbf{u}(\mathbf{x}, t) \tag{5}$$

The force vector state can be expressed as:

$$\mathbf{T} = \underline{C}\,\underline{\mathbf{M}} \tag{6}$$

where $\underline{C}$ is the scalar force state and $\underline{\mathbf{M}}$ is the deformed direction vector state. For ordinary materials, $\underline{\mathbf{M}}$ is given by:[51]

$$\underline{\mathbf{M}} = \begin{cases} \frac{\boldsymbol{\xi}+\boldsymbol{\eta}}{\|\boldsymbol{\xi}+\boldsymbol{\eta}\|} & \text{if } \|\boldsymbol{\xi}+\boldsymbol{\eta}\| \neq 0 \\ 0 & \text{if } \|\boldsymbol{\xi}+\boldsymbol{\eta}\| = 0 \end{cases} \tag{7}$$

In this paper, we adopt the linear peridynamic solid (LPS) constitutive model introduced by Silling *et al.*[51] In this model, the force between pairs of points is assumed to be proportional to the deformation (i.e., linear elastic response) until the fracture point has been reached. The LPS force scalar state is defined as:

$$\underline{C} = \frac{3K\theta}{m}\underline{\omega x} + \frac{15G}{m}\underline{\omega e^d} \tag{8}$$

where m is the weighted volume, $\underline{\omega}$ is a spherical influence function, K is the bulk modulus, G is the shear modulus, θ is the dilatation, and $\underline{e}^d$ is the deviatoric part of the extension scalar state $\underline{e}$. As such, this constitutive model does not account for the effect of permanent densification and shear flow.

In peridynamics, fracture is modeled in terms of the formation of damage, wherein damage is defined at the particle level. In detail, the level of damage of a given particle increases when the bonds it forms with other particles located in its neighborhood start to break. The state (i.e., broken or not) as a given bond depends on its magnitude of stress s, which is defined as:

$$s = \frac{\| \boldsymbol{\xi} + \boldsymbol{\eta} \| - \| \boldsymbol{\xi} \|}{\| \boldsymbol{\xi} \|} \tag{9}$$

Based on this formalism, a given bond breaks when its magnitude of stretch s exceeds a critical stretch value s_c. At this point, the interaction (bond) between these points is permanently removed. For three-dimensional systems governed by the LPS constitutive model, s_c is given by:[31]

$$s_c = \sqrt{\frac{G_c}{\left(3G + \left(\frac{3}{4}\right)^4 \left(K - \frac{5G}{3}\right)\right)\delta}} \tag{10}$$

where G_c is the fracture energy of the modeled material and δ is the horizon.

2.4 Nanoindentation simulation

We use peridynamics to explicitly simulate the whole nanoindentation process by gradually displacing downward and upward the indenter tip so as to mimic the experimental procedure. All simulations are conducted using the Large-scale Atomic/Molecular Massively Parallel Simulator (LAMMPS) package.[52] The details of the simulation are as follows. We consider a cubic glass substrate with dimensions of $4 \times 4 \times 4$ μm^3 (see Fig. 2a). The total number of particles that are used to describe the glass substrate is 454,500. The glass substrate is modeled as being perfectly homogeneous. Indeed, although soda-lime silicate glasses may exhibit some degree of heterogeneity at the atomic scale,[53] the level of heterogeneity becomes neglectable at the length scale that is probed by nanoindentation (i.e., 100s of nm). As illustrated in Fig. S1, load-displacement curves from independent measurements (at different positions on the glass surface) are virtually identical, which suggests that the soda-lime silicate glass considered herein is indeed homogeneous at this length scale. We then model a Berkovich tip as a rigid body that consists of 5,775 particles (see Fig. 2). Here, the geometry of the Berkovich indenter used in our experiments is explicitly mimicked in our peridynamic model according to the parameters that are sourced from Ref.[47] The three-sided pyramid indenter shape is created with a semi-angle between vertical and each face of 65.27° (see Fig. 2). The indenter tip and glass substrate domains are both discretized into small lattice points with a fixed grid spacing of 37.5 nm, which is small enough to observe a convergence of the load-displacement curve.

We parameterize the LPS constitutive model used herein based on available experimental data obtained for soda-lime silicate glasses. In detail, we fix the density at 2.50 g/cm^3,[54] the Poisson's ratio at 0.23,[55] and the fracture energy at 3.5 J/m^2.[53] Regarding the value of the Young's modulus used herein, we deliberately chose to use as input the indentation modulus obtained the present nanoindentation test to estimate the Young's modulus of the glass (rather than using previously reported Young's modulus values obtained with alternative methods). This aims to ensure a meaningful comparison between simulations and experiments. This allows us to ensure that the Young's modulus value used as input for the present constitutive model (i) is compatible with the composition of the glass that is experimentally tested herein (since the composition of a soda-lime silicate glass is not universal), (ii) matches the degree of annealing of the glass considered herein (since annealing and fictive temperature can affect the Young's modulus), and (iii) that the present Young's modulus is compatible with nanoindentation data (since different techniques, e.g., ultrasonic resonance, fiber bending, or indentation may yield different stiffness values). Here, in detail, we determine the Young's modulus E of the glass (79 GPa) based on the following formula:[56]

$$\frac{1}{M} = \frac{\left(1-\nu_{\mathrm{i}}^2\right)}{E_{\mathrm{i}}} + \frac{\left(1-\nu^2\right)}{E} \tag{11}$$

where M is the glass's indentation modulus that is experimentally measured herein by nanoindentation (77.9 GPa), ν is the glass's Poisson's ratio (0.23), while E_{i} (1141 GPa) and ν_{i} (0.07) represent the Young's modulus and Poisson's ratio of the indenter, respectively.

This constitutive model yields a bulk modulus K = 48.8 GPa, a shear modulus G = 32.1 GPa, and a critical stretch s_{c} = 0.0181. In line with previous studies, the horizon distance is set to be three times the grid spacing.[57] Periodic boundary conditions are applied in the X- and Z- directions while the Y direction (i.e., loading direction) is set to be non-periodic. The bottom three layers are fixed in space to serve as the boundary to anchor the glass substrate.

Nanoindentation is then modeled by vertically displacing the indenter tip toward the glass substrate. The load is computed as the resultant force applied by the indenter on the glass substrate (or vice versa). In detail, we record all the individual force components imposed on the indenter at a given time and sum them up to calculate the resultant force. The tip is first displaced downward with a fixed velocity of 0.25 m/s (loading) until the maximum penetration depth (400 nm) is

reached, and subsequently displaced upward with the same fixed velocity (unloading). Artificial damping is introduced by using a Nosé–Hoover thermostat.[58] The timestep is fixed at 0.75 ps, which is small enough to ensure the stability of the simulation based on a von Neumann stability analysis.[59] Figure 2b shows the topography of the surface of the indented glass at maximum loading.

2.5 Uniaxial compression simulation

To further validate our constitutive model, we conduct a uniaxial compression simulation of the same soda-lime silicate glass and compare our simulated data with available experimental results from Ref.[60] To this end, we simulate an 800 × 800 × 800 nm cubic system and subject it to a uniaxial compression along the *Y*-axis. This system size is found to be large enough to ensure a convergence of the obtained stress-strain curve. To ensure consistency, all simulation details (e.g., timestep, lattice size, constitutive model, etc.) are kept identical to those used in the indentation simulations. The deformation is conducted by gradually deforming the simulation box along the *Y*-axis, with a deformation rate of 2×10^4 s^{-1}, which is found to be low enough to yield a convergence of the computed stress-strain curve. Stress is maintained at zero along the lateral directions (*X*- and *Z*-axis).

3. Results

3.1 Effects of indenter velocity and system size

We first focus on the effect of the indenter displacement velocity on the load-displacement curves obtained in simulations. Indeed, although using the experimental displacement velocity in the peridynamic simulations would be ideal, this timescale would far exceed the timescale that is accessible to peridynamic simulations with the timestep considered herein. Here, we assess the influence of the displacement velocity of the indenter on the computed load-displacement curve to ensure that the selected velocity is small enough to avoid resulting in any spurious effects. To this end, we gradually decrease the displacement velocity from 1.5 down to 0.15 m/s while maintaining constant all the other parameters (including the maximum penetration depth). Figure 3a shows the computed load-displacement curves associated with varying displacement velocities. We first note

that, as expected, the obtained load-displacement curve exhibits a convex shape and is non-reversible, in agreement with typical experimental nanoindentation results (see Fig. 1). We then observe that the vertical displacement velocity of the indenter tip has a notable influence of the resulting load-displacement curve. In detail, we find that larger displacement velocities result in lower loads (see Fig. 3b). Notably, the maximum indentation load decreases by about 35 % as the displacement velocity increases from 0.15 to 1.5 m/s. Based on this observation, we fix the velocity of the indenter tip at 0.25 m/s in the following simulations to achieve the best balance between accuracy and computational efficiency.

Next, we focus on the effect of the system size on the simulated load-displacement curves, so as to ensure that the simulated system is large enough to avoid any spurious effects of the boundary domain. To this end, we simulate the indentation of a series of cubic glass substrates with varying length ranging from 2.5 to 4.5 μm. Figure 4a shows the resulting load-displacement curves. As expected, we observe that the resulting load-displacement curve is notably affected by the size of the system, which further motivates the need to conduct large-scale peridynamic simulation rather than smaller scale MD simulations to study the mechanical response of glasses upon indentation. In detail, we find that, at fixed displacement, the computed load tends to drop as the simulated system becomes smaller (see Fig. 4b). This can be understood from the fact that, in the case of very small systems, the dimension of the glass domain that is affected by indentation (that is, wherein stress and strain develop) eventually exceeds the size of the sample itself. Furthermore, the assumption of plane strain, which the Oliver and Pharr model is based on, is not valid for domains with small dimensions. In addition, we observe that smaller systems tend to exhibit larger load fluctuations during indentation (see Fig. 3a).

Nevertheless, we observe that, when the system becomes large enough (i.e., with a dimension equal or larger than 4 μm), the computed load-displacement curve remains largely constant. This indicates that, in this regime, the simulated glass is large enough to avoid any finite-size effect. Based on this observation, we fix the dimensions of the glass substrate at 4 μm in the following simulations to ensure maximum computational efficiency. We observe some fluctuations in the simulated load-displacement curves showing above. It should be noted that this fluctuation is not significantly affected by loading rate but becomes less pronounced in larger simulated systems

(see Supplementary Materials). Such load fluctuations likely originate from the interaction among the stress waves released upon bond breaking.

3.2 Comparison between peridynamic and experimental results

Having ensured that the simulation parameters are properly optimized to achieve satisfactory accuracy and computational efficiency, we now compare the computed load-displacement curve with the experimental nanoindentation data obtained herein (see Fig. 5). Overall, we observe a good agreement between simulated and experimental data, both during the loading and unloading phases. Note that the computed results are not based on any fitting parameters and simply depend on the constitutive model parameters (i.e., Young's modulus, Poisson's ratio, and fracture energy).

In detail, we find that the computed load is largely similar to the experimental data during the loading phase. In this phase, we note that the system exhibits fairly large load fluctuations, especially at high penetration depth. Such fluctuations likely arise from sudden releases in kinetic energy when bonds break and, hence, become notably smaller upon unloading. We note that the simulation slightly overestimates the load at the maximum penetration depth. This may arise from the fact that the constitutive model used herein is purely linear elastic until fracture initiates and, hence, does not comprise any plastic or viscous behaviors (which would be needed to model shear flow and densification). [61] Nevertheless, the overall harmony between simulated and experimental results suggest that the irreversible deformation that controls the load-displacement curve can be modeled in terms of bond breaking. We then note that the slope of the load-displacement curve upon unloading is properly reproduced, which suggests that the peridynamic simulation properly describes the stiffness of the glass (which governs its elastic recovery upon unloading).

Importantly, we observe that the overall degree of irreversibility of the indentation process (i.e., as captured by the residual penetration depth under zero load after unloading) is fairly well reproduced (although slightly underestimated) by the peridynamic simulation. This denotes that, despite solely relying on a simple LPS constitutive model, the peridynamic simulation properly describes the magnitude of energy dissipation during the loading/unloading process, which is captured by the area under the load-displacement curve.[62] In turn, this suggests that, in this case, the main irreversible, inelastic behaviors that govern the load-displacement curve can simply be

modeled in terms of the existence of a certain number of interparticle bonds that irreversibly and instantly break once the magnitude of their stretch exceeds the critical stretch value.

Altogether, due to the overall harmony between the simulated and experimental load-displacement curves, the values of the indentation hardness and modulus extracted by the Oliver and Pharr method from the simulation data are comparable to the experimental values (see Fig. 5)—although the fact that the computed indentation stiffness agrees with the experimental data is not surprising since this property is used to inform the LPS constitutive model. This overall agreement denotes that, despite the simplicity of the constitutive model used herein, peridynamics offers an attractive pathway to simulate the mechanical response of silicate glasses to nanoindentation.

As an additional assessment of our peridynamic simulation, we then compare the topography of the permanently deformed indented glass surface (i.e., after loading and unloading) with experimental data obtained by AFM (see Fig. 6a). As shown in Fig. 6b, we observe a good agreement between simulated and experimental surface topography, both in terms of deformed surface shape and vertical displacement magnitude. Nevertheless, we note that our simulation slightly underestimates the maximum depth of the deformed surface, which echoes the fact that the residual penetration depth is underestimated in the simulation (see Fig. 5). This likely arises from the fact that permanent densifications are not accounted for in the present LPS constitutive model. In addition, experiments suggest the existence of some small indentation pile-ups on both edges of the indent, which are not reproduced by our simulation. This is not surprising, as such pile-ups form through volume-conserving shear flow, which is not accounted for by the LPS constitutive model. It should be noted that, unlike silica glass, no significant sink-in is here experimentally observed during the nanoindentation of soda-lime silicate glasses.

3.3 Observation of stress and damage field under the indenter tip.

Having ensured that our peridynamic simulation yields a satisfactory agreement with experimental data, we further analyze the simulation to access some information that is challenging to experimentally measured, e.g., the stress field that is generated in the glass under the indenter tip—which is a direct outcome of the simulation. In this study, the stress is calculated based on the formula introduced in Ref.[63] In the following, we focus on the spatial distribution of various stress

components observed at the maximum penetration depth (i.e., 400 nm), both along the horizontal *X-Z* plane (i.e., normal to indenter displacement to assess the stress field along the plane of the contact surface) and Y-Z plane (i.e., orthogonal to the contact surface to assess the stress field generated within the bulk of the glass). These axes are illustrated in Fig. 2. We note that no significant velocity wave propagation that would affect the results is observed herein (not shown here).

Figure 7 shows the radial and tangential stress components in the *X-Z* horizontal plane, that is, the plane along which the indenter tip enters in contact with the glass substrate. As expected, we observe that the resulting stress is localized at the vicinity of the indenter. We also note that the stress distribution in the central contact region is fairly heterogeneous, due to the existence of some localized damage (see below). Based on the analysis of the radial component of stress (Fig. 7a), indentation results in the formation of a state of local radial compression (negative stress) near the edges of the indenter and, in turn, a localized state of radial tension (positive stress) at the vicinity of the three corners. In contrast, the tensile and compressive nature of the tangential local stress is reversed, as compared to the radial stress (Fig. 7b). These results match with previous experimental data.[64] In addition, the butterfly-like shape of the stress distribution is similar to the elastic stress distribution obtained by micro-Raman mapping analysis in silicon.[19]

Further, Figure 8 shows the hydrostatic and von Mises stress components in the *Y-Z* vertical plane (i.e., within the bulk of the glass). Again, we observe that the generated stress is primarily localized at the vicinity of the points of contact with the indenter, wherein structural changes have been shown to be the most pronounced.[65] This observation is in agreement with previous simulation results.[16, 66, 67] As expected, we observe that indentation induces a state of hydrostatic compression (negative stress) within the bulk of the glass. The compressive nature of the hydrostatic stress is consistent with previous FEM findings.[68] Such hydrostatic compressive stress is likely to result in the appearance of permanent densification in glasses featuring an open structure (e.g., SiO_2), albeit to a lower extent in glasses exhibiting a compact atomic network.[20] Moreover, we observe the existence of some localized region exhibiting high von Mises shear stress. Such stress could initiate some volume-conservative shear flow within the glass. A more elaborated constitutive model capturing plastic yield and viscous effects would be needed to specifically account for these behaviors.

Finally, we analyze the level of damage forming in the glass during indentation, which is another direct outcome of peridynamics simulations. Figure 9 shows the computed damage contours on the glass surface (in the *X*-*Z* plane) for a load of 10 mN, 12.5 mN, and 17 mN (i.e., during loading), as well as for a load of 10 mN, 5 mN, and 0 mN (i.e., during unloading). Note that a damage value of 1 is indicative of a particle wherein all bonds with neighboring particles are broken, while a damage value of 0.5 corresponds to a particle for which half of the bonds are broken, which is typically considered as a threshold that is indicative of the existence of a crack. Overall, we observe that indentation results in the formation of some localized damage, especially at the center of the indent and at the three corners of the Berkovich tip. Such damage arises from the local stress concentration resulting from the contact with the Berkovich tip (see Fig. 7). We note that the high damage forming at the center of the indent is responsible for the fairly heterogeneous stress field that is obtained within the surface of contact with the indenter (see Fig. 7).

The formation of such damage is here not surprising, since damage (i.e., bond breaking) is the only form of non-linearity in the present LPS model that can explain the non-reversibility of the load-displacement curve. Nevertheless, this damage remains highly localized (limited to the near vicinity of the contact point with the indenter tip) and does not result in the formation of a macroscopic crack. It should be noted that, here, damage may act as a proxy that indirectly captures the non-linear deformation of the glass under indentation, which would otherwise occur through shear flow or permanent densification in real glasses. As such, the damage that is observed herein may not directly translate into a clear physical reality in actual glasses subjected to indentation.

4. Discussion

Finally, we discuss the limitations of the present constitutive model, as well as the origin of the satisfactory agreement with experimental data. Indeed, as mentioned above, plastic deformations are not considered in the LPS constitutive model used herein. As such, it is notable that our simulations can offer a good prediction of the load-displacement curve, indentation modulus, and hardness as compared with experimental data despite the fact that shear flow and permanent densification are not accounted for in the present LPS constitutive model. Moreover, transient elastic properties and their spatial distribution are also not considered in the present LPS

constitutive model. In the following, we further explore the reasons according to which we nevertheless obtain a satisfactory agreement with experimental data while relying on an incomplete description of the behavior of the glass under load.

We first focus on shear flow, which manifests itself by a volume-conserving displacement of matter.[69] Shear flow is expected to play an important role in governing the response to indentation of soda-lime silicate glasses[17] and, indeed, its existence is supported by the present nanoindentation experiment, which shows the formation of pile-ups on each edge of the indent (see Fig. 6). However, we note that the height of such pile-ups remains small as compared to those that, for instance, are observed in bulk metallic glasses.[70] The limited extent of such pile-ups likely explains why our simulation is able to predict a post-indentation surface topography that matches fairly well with experimental data without explicitly accounting for shear flow deformations. Similarly, the effect of associated transient elastic properties is also expected to be limited. Although including shear flow effects and associated transient elastic properties in the constitutive model would be desirable, this is a fairly complex task due to the lack of available glass rheology data under such high stress.

Next, we focus on permanent densification. To assess whether the stress that is forming within the glass during indentation (see Fig. 8) is intense enough to induce permanent densification, we consider, as a reference, some experimental data obtained by subjecting a soda-lime silicate glass to uniaxial compression.[60] We then replicate this deformation by peridynamic simulation (see Methods), which allows us to *a posteriori* assess the reliability of our LPS constitutive model. In particular, this allows us to determine at which stress our constitutive model starts to deviate from experimental data, that is, when permanent densification becomes activated within the compressed glass.

Figure 10 shows a comparison between the simulated and experimental stress as a function of the relative volume of the glass upon uniaxial loading. First, we observe a very good agreement between simulation and experiments at moderate stress (< 6 GPa). This indicates that, in this regime, our LPS constitutive model properly reproduces the linear elastic response of soda-lime silicate glasses. This also *a posteriori* supports the choice of the Young's modulus value that is adopted herein. However, upon higher stress (> 6 GPa), we observe a clear deviation between simulation and experimental results, wherein the experimental data exhibit a deviation from

linearity that is not captured by the present simulation. This indicates that, at this point, the glass starts to exhibit some non-linear, irreversible permanent densification, which is not accounted for by the LPS constitutive model. Although this is a clear limitation of the LPS model, we note that this critical stress at which the onset of permanent densification is observed remains high as compared to the magnitude of the stress generated within the glass by indentation (see Fig. 8). Specifically, we observe that, for the range of indentation loads considered herein, the local stress resulting from indentation mostly remains below 6 GPa (except at the immediate vicinity of the contact point with indenter). This indicates that, based on the stress contours predicted herein by peridynamics (see Fig. 8), permanent densification is expected to remain very localized and concentrated near the contact surface with the indenter. This echoes the fact that, unlike pure silica, soda-lime silicate glasses exhibit a highly-packed atomic structure, since Na and Ca network formers occupy the interatomic spacing between the network formers that is otherwise left empty in pure silica.[71] Consequently, the packed atomic structure of soda-lime silicate exhibits a lower propensity for permanent densification than silica.[71] This *a posteriori* explains why our model predicts a fairly realistic load-displacement curve without explicitly accounting for permanent densification. Nevertheless, incorporating permanent densification in the constitutive model will ultimately certainly be desirable to offer a more complete, realistic description of glass indentation.

5. Conclusions

Altogether, this study demonstrates that, based on the sole knowledge of the constitutive model parameters (Young's modulus, shear modulus, and fracture energy), peridynamic simulations offers a good match with nanoindentation experimental data, both in terms of load-displacement curve and indentation stiffness/hardness. It is notable that peridynamics properly captures the irreversible nature of indentation-induced deformations while relying on a simple linear-elastic constitutive model, wherein damage is the only form of non-linearity. Nevertheless, further investigation of the influence of shear flow and densification, based on more complex and realistic constitutive models, will be extremely valuable. Overall, this study establishes peridynamics as a promising method to simulate the mechanical response of oxide glasses upon indentation and, in turn, can be used to revel some details (e.g., the stress field at a given state of stress, size of activated elastic volume, individual contribution of elastic and inelastic deformation, etc.) that are

otherwise challenging to access experimentally. This knowledge is required to further decipher the underlying physics governing the response of glasses to indentation and, more generally, to inform the discovery of novel glasses with improved mechanical resistance when subjected to concentrated loads.

Declaration of Competing Interest

The authors declare that they have no known competing financial interests or personal relationships that could have appeared to influence the work reported in this paper.

Acknowledgments

This work was supported by the National Science Foundation (under Grants No. 1826420 and 1826050).

References

1. Gibson RF. A review of recent research on nanoindentation of polymer composites and their constituents. *Compos Sci Technol*. 2014;105:51–65. https://doi.org/10.1016/j.compscitech.2014.09.016
2. Liu Y, Wang B, Yoshino M, Roy S, Lu H, Komanduri R. Combined numerical simulation and nanoindentation for determining mechanical properties of single crystal copper at mesoscale. *J Mech Phys Solids*. 2005;53(12):2718–2741. https://doi.org/10.1016/j.jmps.2005.07.003
3. Lucca DA, Herrmann K, Klopfstein MJ. Nanoindentation: Measuring methods and applications. *CIRP Ann*. 2010;59(2):803–819. https://doi.org/10.1016/j.cirp.2010.05.009
4. Miller M, Bobko C, Vandamme M, Ulm F-J. Surface roughness criteria for cement paste nanoindentation. *Cem Concr Res*. 2008;38(4):467–476. https://doi.org/10.1016/j.cemconres.2007.11.014

5. Zhu TT, Bushby AJ, Dunstan DJ. Size effect in the initiation of plasticity for ceramics in nanoindentation. *J Mech Phys Solids*. 2008;56(4):1170–1185. https://doi.org/10.1016/j.jmps.2007.10.003
6. Liu K, Ostadhassan M, Bubach B. Applications of nano-indentation methods to estimate nanoscale mechanical properties of shale reservoir rocks. *J Nat Gas Sci Eng*. 2016;35:1310–1319. https://doi.org/10.1016/j.jngse.2016.09.068
7. Oliver WC, Pharr GM. An improved technique for determining hardness and elastic modulus using load and displacement sensing indentation experiments. *J Mater Res*. 1992;7(6):1564–1583. https://doi.org/10.1557/JMR.1992.1564
8. Broitman E. Indentation Hardness Measurements at Macro-, Micro-, and Nanoscale: A Critical Overview. *Tribol Lett*. 2017;65(1):23. https://doi.org/10.1007/s11249-016-0805-5
9. Lawn BR. Indentation of Ceramics with Spheres: A Century after Hertz. *J Am Ceram Soc*. 1998;81(8):1977–1994. https://doi.org/10.1111/j.1151-2916.1998.tb02580.x
10. Miura T, Benino Y, Sato R, Komatsu T. Universal hardness and elastic recovery in Vickers nanoindentation of copper phosphate and silicate glasses. *J Eur Ceram Soc*. 2003;23(3):409–416. https://doi.org/10.1016/S0955-2219(02)00154-1
11. Kese KO, Li ZC, Bergman B. Method to account for true contact area in soda-lime glass during nanoindentation with the Berkovich tip. *Mater Sci Eng A*. 2005;404(1):1–8. https://doi.org/10.1016/j.msea.2005.06.006
12. Gong J, Miao H, Peng Z. On the contact area for nanoindentation tests with Berkovich indenter: case study on soda-lime glass. *Mater Lett*. 2004;58(7):1349–1353. https://doi.org/10.1016/j.matlet.2003.09.026
13. Morris DJ, Cook RF. In Situ Cube-Corner Indentation of Soda–Lime Glass and Fused Silica. *J Am Ceram Soc*. 2004;87(8):1494–1501. https://doi.org/10.1111/j.1551-2916.2004.01494.x
14. Evans AG, Wilshaw TR. Dynamic solid particle damage in brittle materials: an appraisal. *J Mater Sci*. 1977;12(1):97–116. https://doi.org/10.1007/BF00738475
15. Marshall DB, Evans AG, Nisenholz Z. Measurement of Dynamic Hardness by Controlled Sharp-Projectile Impact. *J Am Ceram Soc*. 1983;66(8):580–585. https://doi.org/10.1111/j.1151-2916.1983.tb10095.x

16. Januchta K, Smedskjaer MM. Indentation deformation in oxide glasses: Quantification, structural changes, and relation to cracking. *J Non-Cryst Solids X*. 2019;1:100007. https://doi.org/10.1016/j.nocx.2018.100007
17. Barthel E, Keryvin V, Rosales-Sosa G, Kermouche G. Indentation cracking in silicate glasses is directed by shear flow, not by densification. *Acta Mater*. 2020;194:473–481. https://doi.org/10.1016/j.actamat.2020.05.011
18. Kasimuthumaniyan S, Reddy AA, Krishnan NMA, Gosvami NN. Understanding the role of post-indentation recovery on the hardness of glasses: Case of silica, borate, and borosilicate glasses. *J Non-Cryst Solids*. 2020;534:119955. https://doi.org/10.1016/j.jnoncrysol.2020.119955
19. Ma L, Xing H, Ding Q, Han Y, Li Q, Qiu W. Analysis of residual stress around a Berkovich nano-indentation by micro-Raman spectroscopy. *AIP Adv*. 2019;9(1):015010. https://doi.org/10.1063/1.5080179
20. Fuhrmann S, de Macedo GNBM, Limbach R, *et al.* Indentation-Induced Structural Changes in Vitreous Silica Probed by in-situ Small-Angle X-Ray Scattering. *Front Mater*. 2020;7. https://doi.org/10.3389/fmats.2020.00173
21. Landman U, Luedtke WD, Burnham NA, Colton RJ. Atomistic Mechanisms and Dynamics of Adhesion, Nanoindentation, and Fracture. *Science*. 1990;248(4954):454–461. https://doi.org/10.1126/science.248.4954.454
22. Ma X-L, Yang W. Molecular dynamics simulation on burst and arrest of stacking faults in nanocrystalline Cu under nanoindentation. *Nanotechnology*. 2003;14(11):1208–1215. https://doi.org/10.1088/0957-4484/14/11/009
23. Li J, Van Vliet KJ, Zhu T, Yip S, Suresh S. Atomistic mechanisms governing elastic limit and incipient plasticity in crystals. *Nature*. 2002;418(6895):307–310. https://doi.org/10.1038/nature00865
24. Reddy JN. An introduction to the finite element method. 3rd ed. New York, NY: McGraw-Hill Higher Education; 2006
25. Imaoka M, Yasui I. Finite element analysis of indentation on glass. *J Non-Cryst Solids*. 1976;22(2):315–329. https://doi.org/10.1016/0022-3093(76)90062-4

26. Kermouche G, Barthel E, Vandembroucq D, Dubujet Ph. Mechanical modelling of indentation-induced densification in amorphous silica. *Acta Mater*. 2008;56(13):3222–3228. https://doi.org/10.1016/j.actamat.2008.03.010
27. Keryvin V, Charleux L, Hin R, Guin J-P, Sangleboeuf J-C. Mechanical behaviour of fully densified silica glass under Vickers indentation. *Acta Mater*. 2017;129:492–499. https://doi.org/10.1016/j.actamat.2017.03.008
28. Bažant ZP, Oh BH. Crack band theory for fracture of concrete. *Matér Constr*. 1983;16(3):155–177. https://doi.org/10.1007/BF02486267
29. Hillerborg A, Modéer M, Petersson P-E. Analysis of crack formation and crack growth in concrete by means of fracture mechanics and finite elements. *Cem Concr Res*. 1976;6(6):773–781. https://doi.org/10.1016/0008-8846(76)90007-7
30. Zi G, Belytschko T. New crack-tip elements for XFEM and applications to cohesive cracks. *Int J Numer Methods Eng*. 2003;57(15):2221–2240. https://doi.org/10.1002/nme.849
31. Madenci E, Oterkus E. Peridynamic Theory and Its Applications. New York: Springer-Verlag; 2014 https://doi.org/10.1007/978-1-4614-8465-3
32. Silling SA, Askari E. A meshfree method based on the peridynamic model of solid mechanics. *Comput Struct*. 2005;83(17–18):1526–1535. https://doi.org/10.1016/j.compstruc.2004.11.026
33. Silling SA. Reformulation of elasticity theory for discontinuities and long-range forces. *J Mech Phys Solids*. 2000;48(1):175–209. https://doi.org/10.1016/S0022-5096(99)00029-0
34. Tang L, Krishnan NMA, Berjikian J, *et al.* Effect of nanoscale phase separation on the fracture behavior of glasses: Toward tough, yet transparent glasses. *Phys Rev Mater*. 2018;2(11):113602. https://doi.org/10.1103/PhysRevMaterials.2.113602
35. Rivera J, Berjikian J, Ravinder R, *et al.* Glass Fracture Upon Ballistic Impact: New Insights From Peridynamics Simulations. *Front Mater*. 2019;6. https://doi.org/10.3389/fmats.2019.00239
36. Ha YD, Bobaru F. Studies of dynamic crack propagation and crack branching with peridynamics. *Int J Fract*. 2010;162(1):229–244. https://doi.org/10.1007/s10704-010-9442-4

37. Dipasquale D, Zaccariotto M, Galvanetto U. Crack propagation with adaptive grid refinement in 2D peridynamics. *Int J Fract*. 2014. https://doi.org/10.1007/s10704-014-9970-4
38. Zhou X, Wang Y, Qian Q. Numerical simulation of crack curving and branching in brittle materials under dynamic loads using the extended non-ordinary state-based peridynamics. *Eur J Mech - ASolids*. 2016;60:277–299. https://doi.org/10.1016/j.euromechsol.2016.08.009
39. Ahadi A, Hansson P, Melin S. Indentation of thin copper film using molecular dynamics and peridynamics. *Procedia Struct Integr*. 2016;2:1343–1350. https://doi.org/10.1016/j.prostr.2016.06.171
40. Jingjing Z, Qing Z, Dan H, Feng S. A peridynamic approach for the simulation of calcium silicate hydrate nanoindentation. *Adv Cem Res*. 2016;28(2):84–91. https://doi.org/10.1680/adcr.15.00018
41. Waxman R, Poisl H, Guven I. Peridynamic analysis of indentation and impact of coated and uncoated electro-optical materials. In: Poisl WH, ed. *Window Dome Technol. Mater. XVI*. Baltimore, United States: SPIE; 2019:14. https://doi.org/10.1117/12.2519582
42. Celik E, Oterkus E, Guven I. Peridynamic Simulations of Nanoindentation Tests to Determine Elastic Modulus of Polymer Thin Films. *J Peridynamics Nonlocal Model*. 2019;1(1):36–44. https://doi.org/10.1007/s42102-019-0005-4
43. Sadowski T, Pankowski B. Peridynamical Modelling of Nanoindentation in Ceramic Composites. *Solid State Phenom*. 2016;254:55–59. https://doi.org/10.4028/www.scientific.net/SSP.254.55
44. Mauro JC, Philip CS, Vaughn DJ, Pambianchi MS. Glass Science in the United States: Current Status and Future Directions. *Int J Appl Glass Sci*. 2014;5(1):2–15. https://doi.org/10.1111/ijag.12058
45. Randall NX, Christoph R, Droz S, Julia-Schmutz C. Localised micro-hardness measurements with a combined scanning force microscope/nanoindentation system. *Thin Solid Films*. 1996;290–291:348–354. https://doi.org/10.1016/S0040-6090(96)09184-5
46. Tabor D. Indentation hardness: Fifty years on a personal view. *Philos Mag A*. 1996;74(5):1207–1212. https://doi.org/10.1080/01418619608239720

47. Hay J, Pharr GM. Instrumented Indentation Testing. 2000 https://doi.org/10.31399/asm.hb.v08.a0003273
48. Kazembeyki M, Bauchy M, Hoover CG. New insights into the indentation size effect in silicate glasses. *J Non-Cryst Solids*. 2019;521:119494. https://doi.org/10.1016/j.jnoncrysol.2019.119494
49. Brenner S, Scott R. The Mathematical Theory of Finite Element Methods. 3rd ed. New York: Springer-Verlag; 2008 https://doi.org/10.1007/978-0-387-75934-0
50. Agwai A, Guven I, Madenci E. Predicting crack propagation with peridynamics: a comparative study. *Int J Fract*. 2011;171(1):65–78. https://doi.org/10.1007/s10704-011-9628-4
51. Silling SA, Epton M, Weckner O, Xu J, Askari E. Peridynamic States and Constitutive Modeling. *J Elast*. 2007;88(2):151–184. https://doi.org/10.1007/s10659-007-9125-1
52. Plimpton S. Fast Parallel Algorithms for Short-Range Molecular Dynamics. *J Comput Phys*. 1995;117(1):1–19. https://doi.org/10.1006/jcph.1995.1039
53. Laurent O, Mantisi B, Micoulaut M. Structure and Topology of Soda-Lime Silicate Glasses: Implications for Window Glass. *J Phys Chem B*. 2014;118(44):12750–12762. https://doi.org/10.1021/jp506155p
54. Bansal NP, Doremus RH. Handbook of Glass Properties. Elsevier; 2013
55. PROPERTIES OF SODA-LIME SILICA FLOAT GLASS. Pilkington North America, Inc; 2013
56. MA D, Chung Wo O, Liu J, HE J. Determination of Young's modulus by nanoindentation. *Sci China Ser E Technol Sci*. 2004;47(4):398–408. https://doi.org/10.1360/03ye0590
57. Bobaru F, Hu W. The Meaning, Selection, and Use of the Peridynamic Horizon and its Relation to Crack Branching in Brittle Materials. *Int J Fract*. 2012;176(2):215–222. https://doi.org/10.1007/s10704-012-9725-z
58. Evans DJ, Holian BL. The Nose–Hoover thermostat. *J Chem Phys*. 1985;83(8):4069–4074. https://doi.org/10.1063/1.449071
59. Silling SA, Askari E. A meshfree method based on the peridynamic model of solid mechanics. *Comput Struct*. 2005;83(17):1526–1535. https://doi.org/10.1016/j.compstruc.2004.11.026

60. Renganathan P, Duffy TS, Gupta YM. Hugoniot states and optical response of soda lime glass shock compressed to 120 GPa. *J Appl Phys*. 2020;127(20):205901. https://doi.org/10.1063/5.0010396
61. Perriot A, Vandembroucq D, Barthel E, *et al.* Raman Microspectroscopic Characterization of Amorphous Silica Plastic Behavior. *J Am Ceram Soc*. 2006;89(2):596–601. https://doi.org/10.1111/j.1551-2916.2005.00747.x
62. Malzbender J, de With G. Energy dissipation, fracture toughness and the indentation load–displacement curve of coated materials. *Surf Coat Technol*. 2000;135(1):60–68. https://doi.org/10.1016/S0257-8972(00)00906-3
63. Thompson AP, Plimpton SJ, Mattson W. General formulation of pressure and stress tensor for arbitrary many-body interaction potentials under periodic boundary conditions. *J Chem Phys*. 2009;131(15):154107. https://doi.org/10.1063/1.3245303
64. Assmann A, Foerster CE, Serbena FC. Indentation residual stresses in soda-lime and borosilicate glasses. *J Non-Cryst Solids*. 2019;503–504:197–207. https://doi.org/10.1016/j.jnoncrysol.2018.09.051
65. Januchta K, Youngman RE, Goel A, *et al.* Discovery of Ultra-Crack-Resistant Oxide Glasses with Adaptive Networks. *Chem Mater*. 2017;29(14):5865–5876. https://doi.org/10.1021/acs.chemmater.7b00921
66. Yang Y, Luo J, Huang L, *et al.* Crack initiation in metallic glasses under nanoindentation. *Acta Mater*. 2016;115:413–422. https://doi.org/10.1016/j.actamat.2016.06.001
67. Jia Y-F, Cui Y-Y, Xuan F-Z, Yang F. Comparison between single loading–unloading indentation and continuous stiffness indentation. *RSC Adv*. 2017;7(57):35655–35665. https://doi.org/10.1039/C7RA06491H
68. Ecker W, Keckes J, Krobath M, *et al.* Nanoscale evolution of stress concentrations and crack morphology in multilayered CrN coating during indentation: Experiment and simulation. *Mater Des*. 2020;188:108478. https://doi.org/10.1016/j.matdes.2020.108478
69. Neely JE, Mackenzie JD. Hardness and low-temperature deformation of silica glass. *J Mater Sci*. 1968;3(6):603–609. https://doi.org/10.1007/BF00757906
70. Vaidyanathan R, Dao M, Ravichandran G, Suresh S. Study of mechanical deformation in bulk metallic glass through instrumented indentation. *Acta Mater*. 2001;49(18):3781–3789. https://doi.org/10.1016/S1359-6454(01)00263-4

71. Koike A, Tomozawa M. IR investigation of density changes of silica glass and soda-lime silicate glass caused by microhardness indentation. *J Non-Cryst Solids*. 2007;353(24):2318–2327. https://doi.org/10.1016/j.jnoncrysol.2007.04.006

Figures Captions:

Fig. 1: Schematic representation of a typical nanoindentation load-displacement curve and of the Oliver and Pharr analysis.[7]

Fig. 2: Geometry of the modelled system (a) before loading and (b) for a penetration depth of 400 nm (i.e., maximum loading). The material points are colors based on their vertical displacement along the *Y*-axis.

Fig. 3: Computed (a) load-displacement curve and (b) maximum indentation load for varying indenter tip vertical displacement velocities. System size is fixed at 4 μm.

Fig. 4: Computed (a) load-displacement curves and (b) maximum indentation load for varying glass substrate system sizes. Indenter tip vertical displacement velocity is fixed at 0.25 m/s.

Fig. 5: Load-displacement curves calculated from the peridynamics simulation and experimental nanoindentation test. The resulting indentation modulus (*M*) and hardness (*H*) obtained from the Oliver and Pharr analysis[7] are indicated for comparison.

Fig. 6. (a) Topography of the surface post indentation, as experimentally measured by atomic force microscopy (AFM). (b) Simulated elevation of the permanently deformed surface after indentation along the axis indicated by a black line in panel (a). The data are compared to the experimental data obtained by AFM shown in panel (a). The horizontal dashed line indicates the position of the initial, undeformed surface.

Fig. 7: Spatial distribution of the (a) radial and (b) tangential component of stress in the *X*-*Z* horizontal plane at the maximum penetration depth (penetration depth of 400 nm). The black triangle indicates the extent of the projected contact area with the indenter.

Fig. 8: Spatial distribution of the (a) hydrostatic and (b) Von Mises component of stress in the *Y*-*Z* vertical plane at the maximum penetration depth (penetration depth of 400 nm). The black area indicates the extent of the indenter.

Fig. 9. Damage contours on the glass substrate surface (in the *X*-*Z* plane) during loading for a load of (a) 10 mN, (b) 12.5 mN, and (c) 17 mN (i.e., at maximun load), and unloading for a load of (d) 10 mN, (e) 5 mN, and (f) 0 mN (i.e., permanent damage post indentation). The orange triangle indicates the extent of the projected contact area with the indenter.

Fig. 10. Computed stress experienced by a soda-lime silicate glass subjected to uniaxial compression as a function of the relative volume V/V_0 (where V_0 is the initial volume). Simulated data are compared with experimental data from Ref.[60]

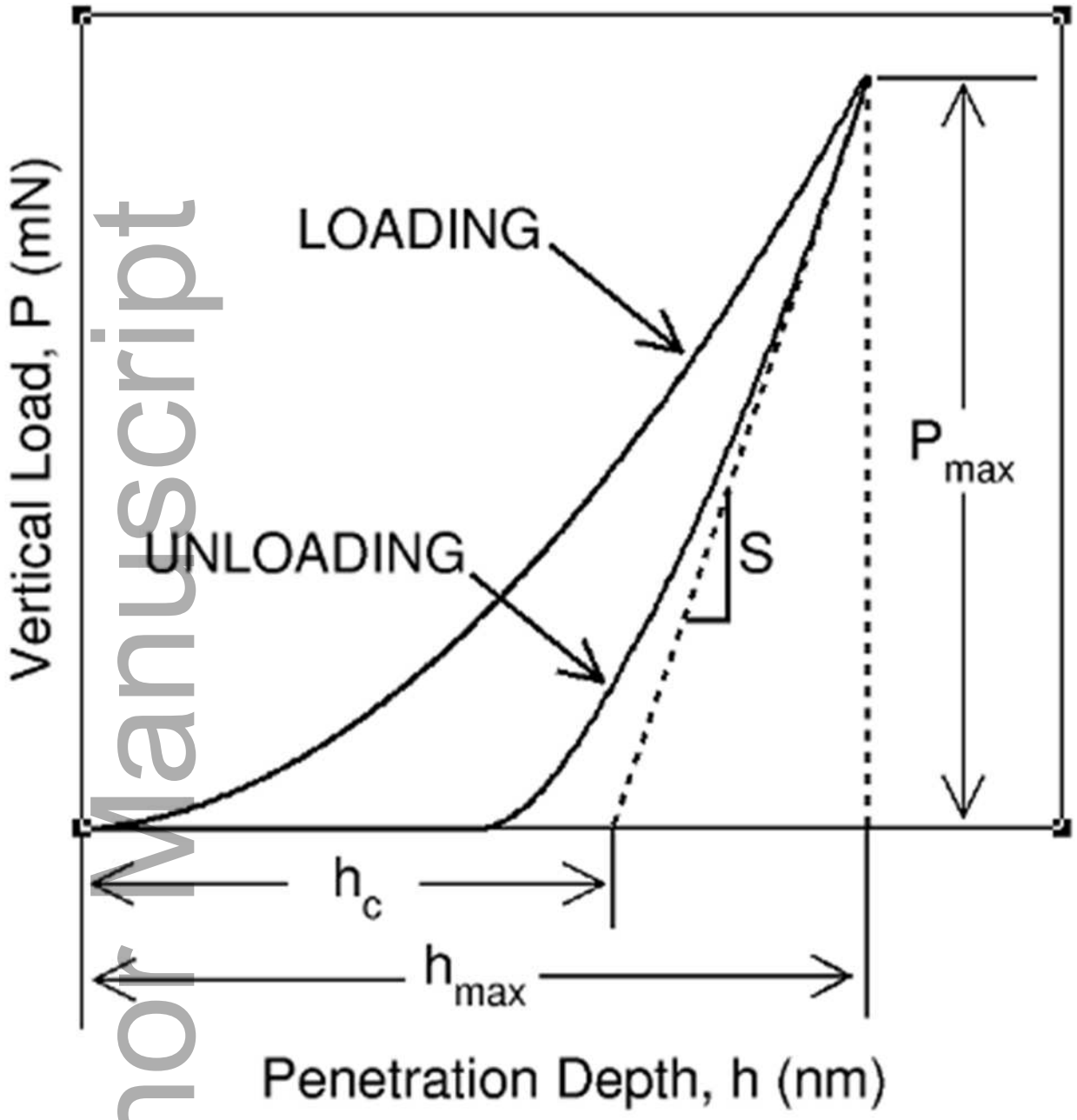

jace_17720_f1.tif

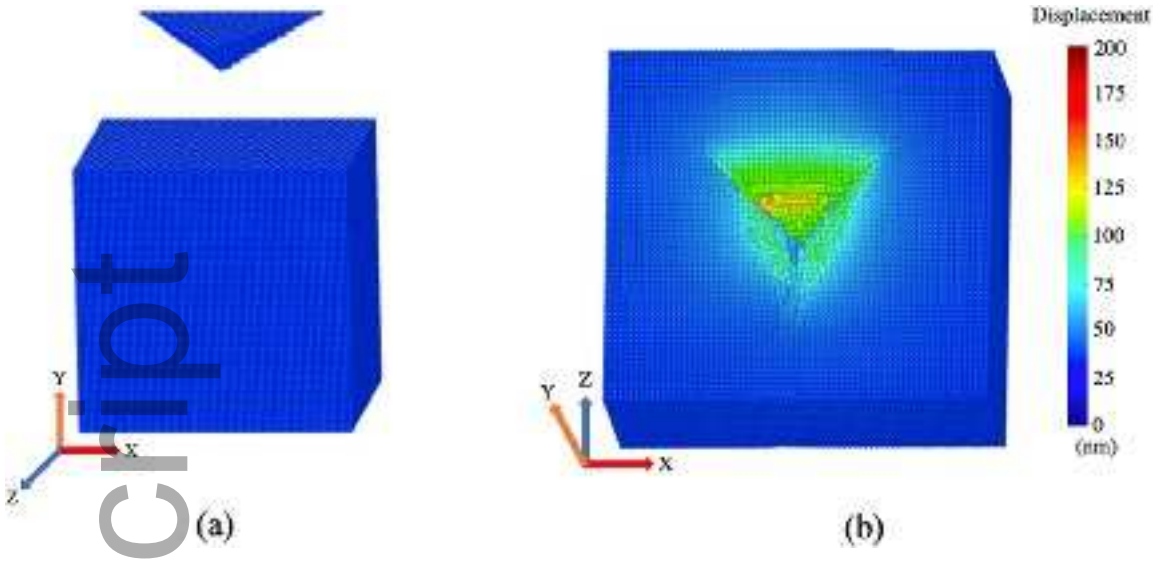

jace_17720_f2.tif

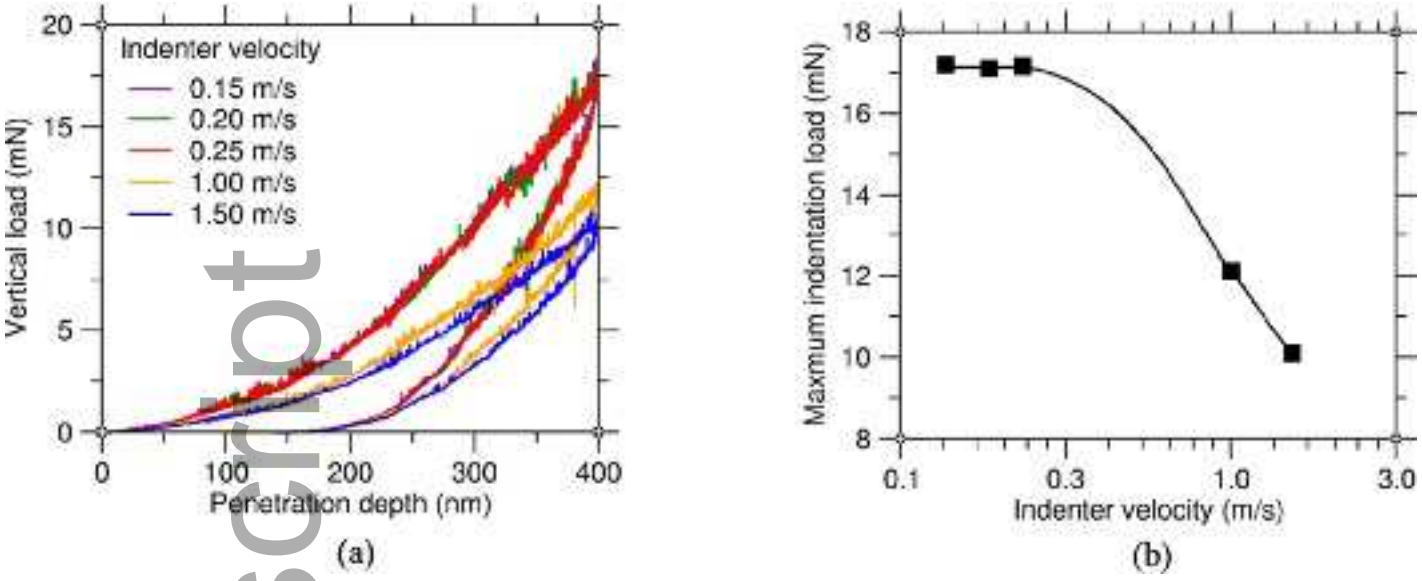

jace_17720_f3.tif

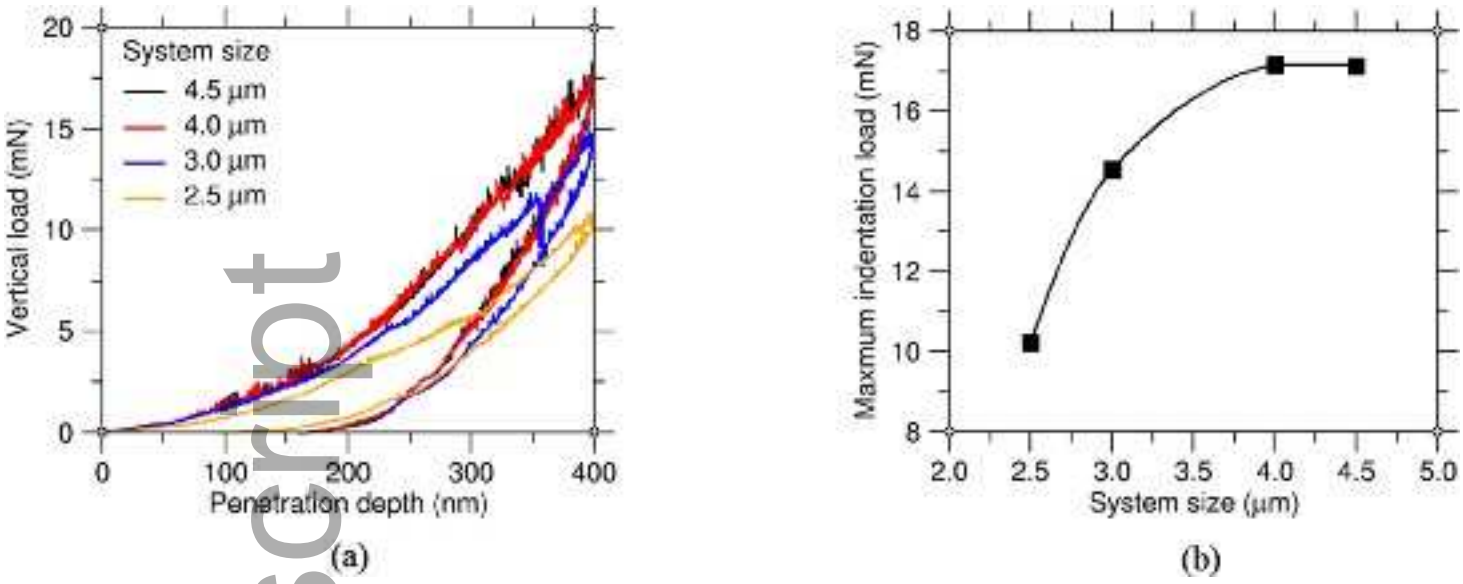

(a) (b)

jace_17720_f4.tif

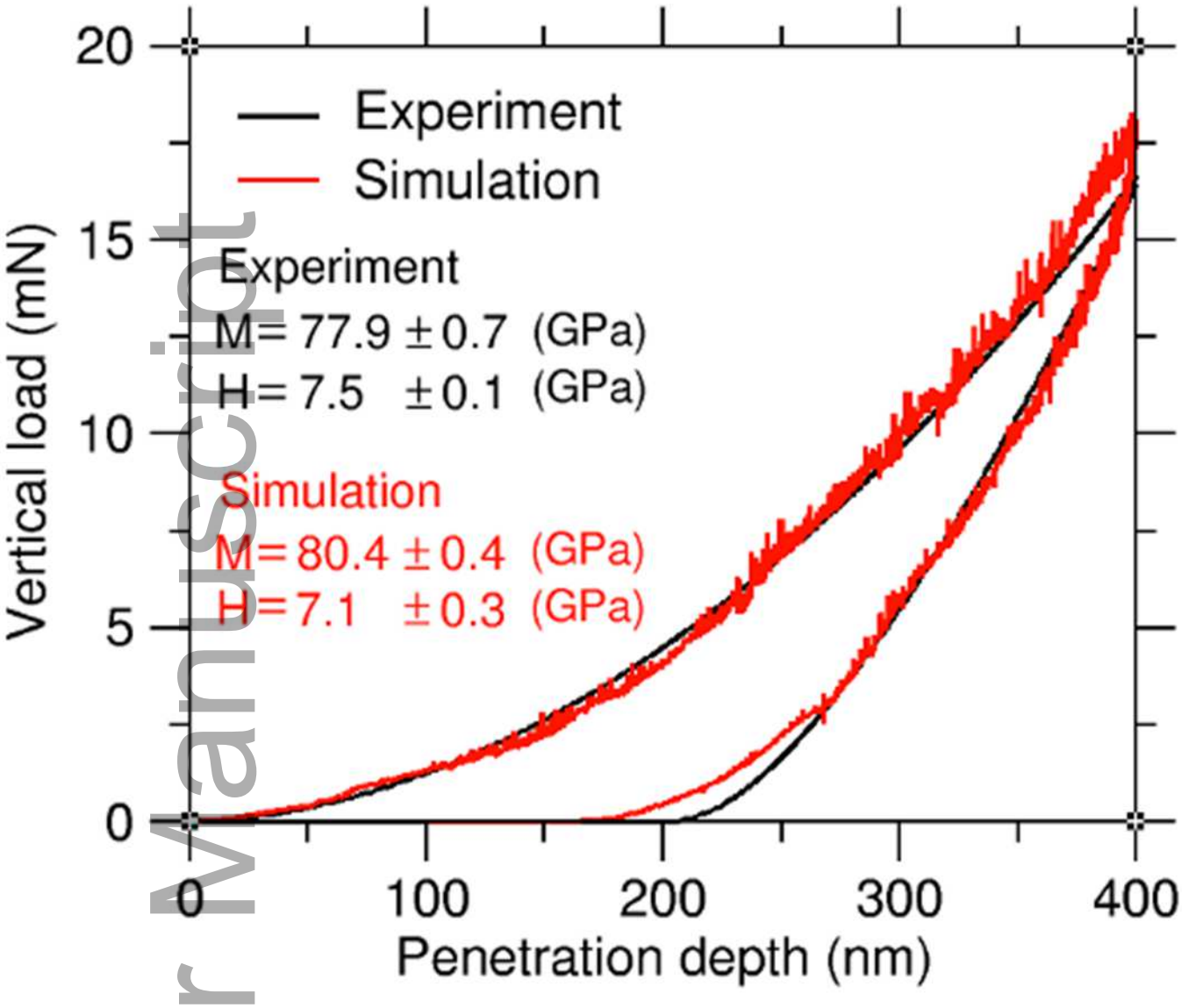

jace_17720_f5.tif

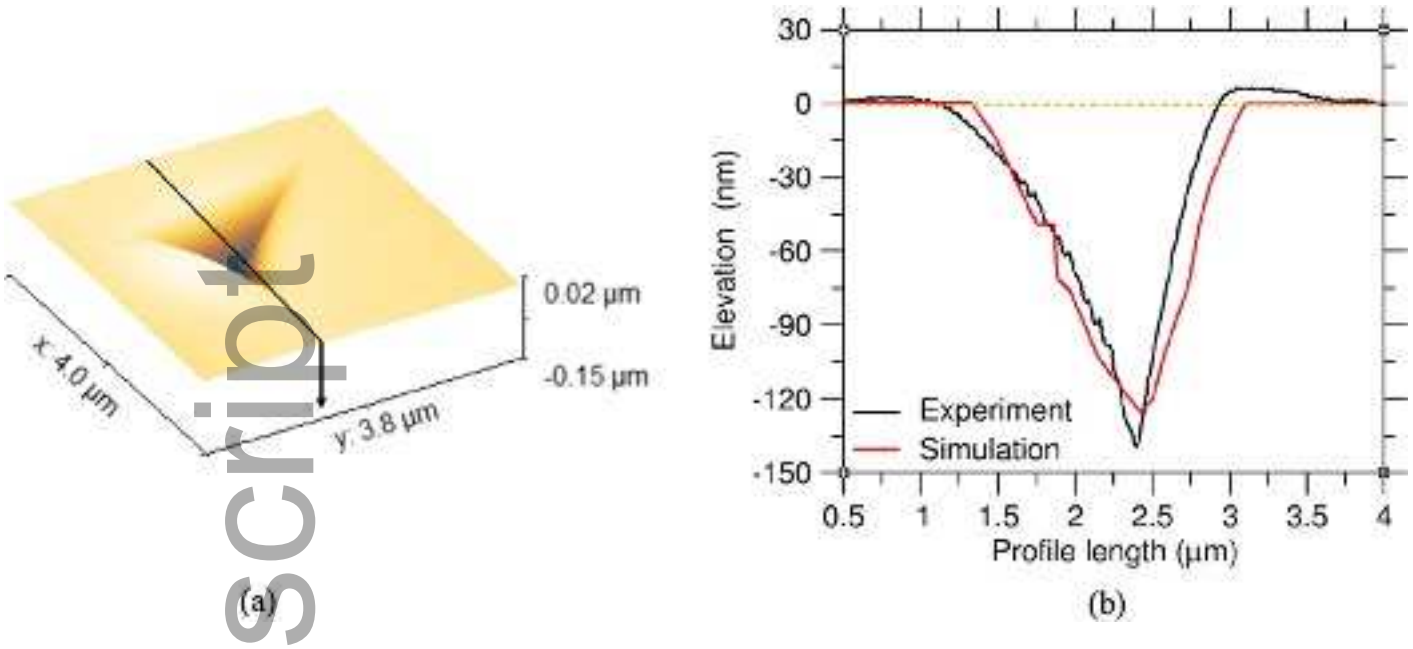

jace_17720_f6.tif

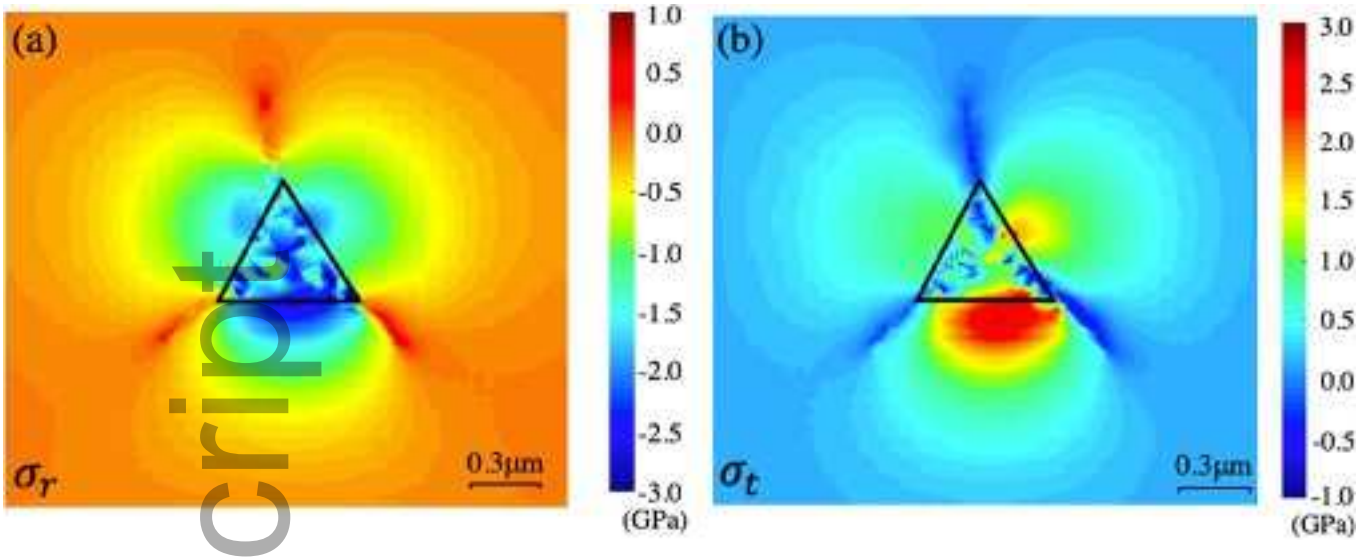

jace_17720_f7.tif

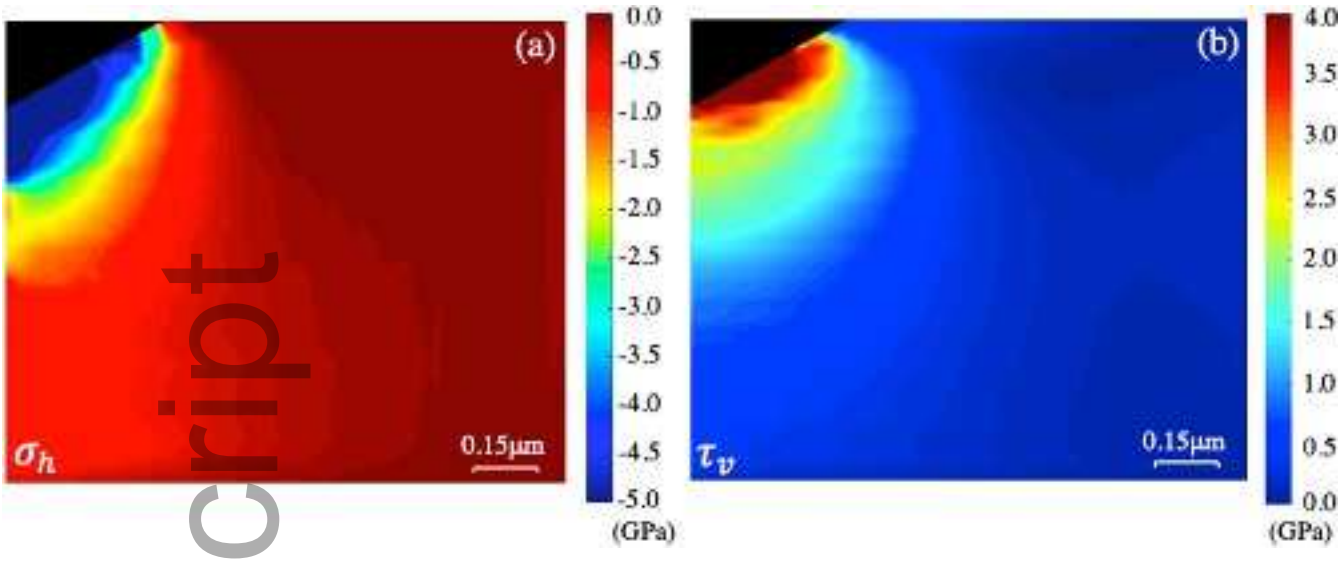

jace_17720_f8.tif

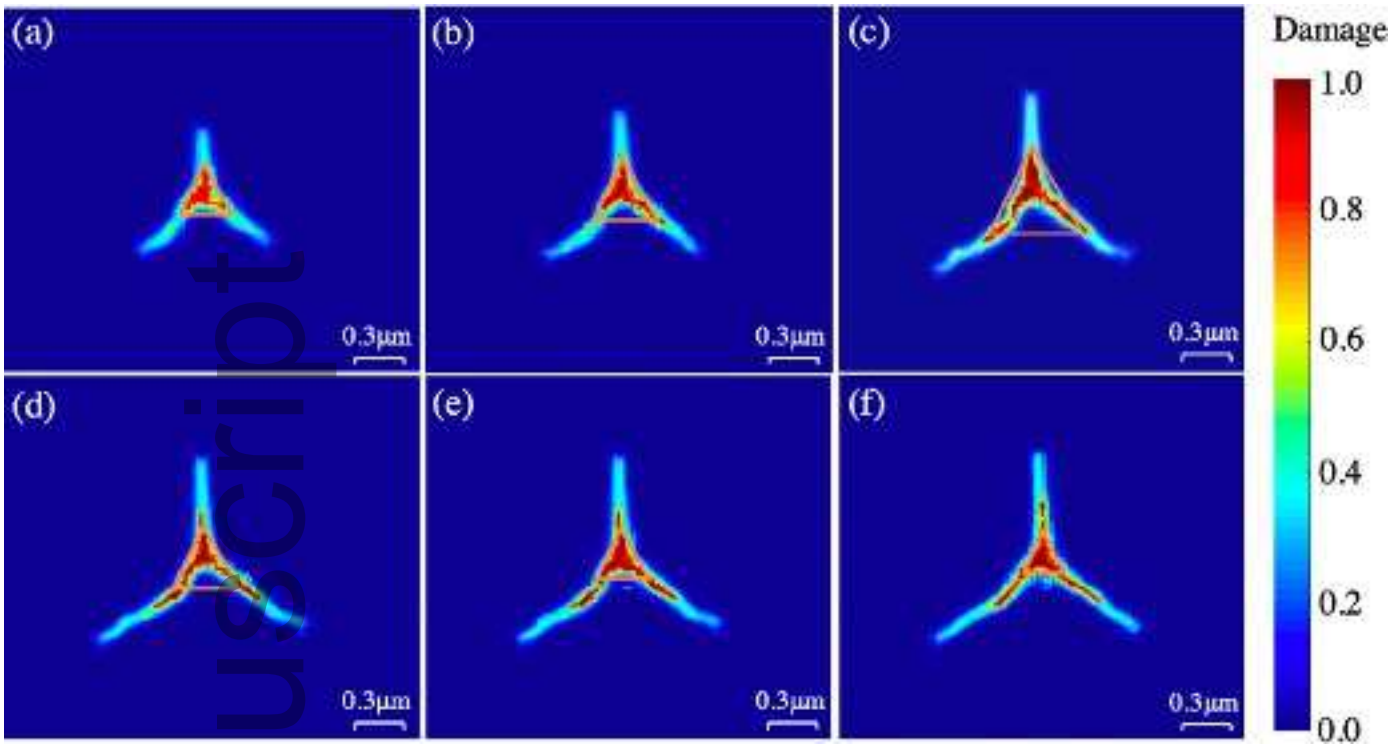

jace_17720_f9.tif

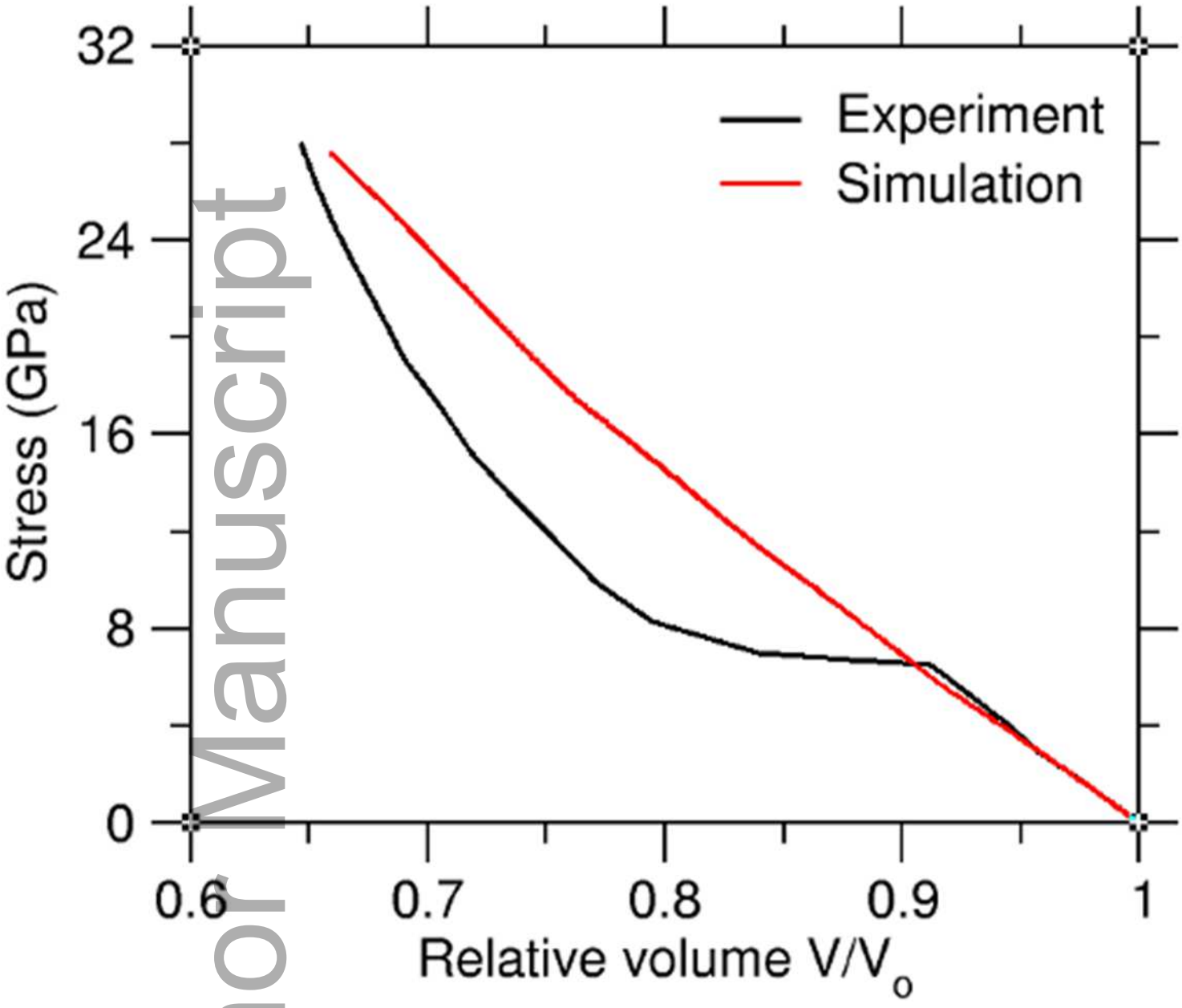

jace_17720_f10.tif